

Ram pressure stripping in elliptical galaxies: I. the impact of the interstellar medium turbulence

Min-Su Shin,^{1*} Mateusz Ruszkowski^{1,2}

¹*Department of Astronomy, The University of Michigan, 500 Church Street, Ann Arbor, MI 48109, USA*

²*The Michigan Center for Theoretical Physics, 3444 Randall Lab, 450 Church St, Ann Arbor, MI 48109, USA*

Accepted ... Received ...; in original form ..

ABSTRACT

Elliptical galaxies contain X-ray emitting gas that is subject to continuous ram pressure stripping over timescales comparable to cluster ages. The gas in these galaxies is not in perfect hydrostatic equilibrium. Supernova feedback, stellar winds, or active galactic nuclei (AGN) feedback can significantly perturb the interstellar medium (ISM). Using hydrodynamical simulations, we investigate the effect of subsonic turbulence in the hot ISM on the ram pressure stripping process in early-type galaxies. We find that galaxies with more turbulent ISM produce longer, wider, and more smoothly distributed tails of the stripped ISM than those characterised by weaker ISM turbulence. Our main conclusion is that even very weak internal turbulence, at the level of $\lesssim 15\%$ of the average ISM sound speed, can significantly accelerate the gas removal from galaxies via ram pressure stripping. The magnitude of this effect increases sharply with the strength of turbulence. As most of the gas stripping takes place near the boundary between the ISM and the intracluster medium (ICM), the boost in the ISM stripping rate is due to the “random walk” of the ISM from the central regions of the galactic potential well to larger distances, where the ram pressure is able to permanently remove the gas from galaxies. The ICM can be temporarily trapped inside the galactic potential well due to the mixing of the turbulent ISM with the ICM. The galaxies with more turbulent ISM, yet still characterised by very weak turbulence, can hold larger amounts of the ICM. We find that the total gas mass held in galaxies decreases with time slower than the mass of the original ISM, and thus the properties of gas retained inside galaxies, such as metallicity, can be altered by the ICM over time. This effect increases with the strength of the turbulence, and is most significant in the outer regions of galaxies.

Key words: hydrodynamics - methods: numerical - galaxies: clusters: general - galaxies: evolution - galaxies: ISM - galaxies: intergalactic medium

1 INTRODUCTION

Ram pressure stripping removes gas from galaxies moving relative to the ICM (Gunn & Gott 1972). Numerous theoretical studies examined the consequences of this effect for the galaxy and cluster evolution by quantifying the amount of gas loss from galaxies, including star formation in galaxies and their ram-pressure stripping tails, and determining the metal enrichment of the ICM by stripping metal-rich gas from galaxies (e.g., Balsara et al. 1994; Domainko et al. 2006; Mayer et al. 2006; Hester 2006; Roediger & Brüggén 2007; Tonnesen et al. 2007; McCarthy et al. 2008; Roediger & Brüggén 2008; Tonnesen & Bryan 2008; Kapferer et al.

2008, 2009; Jáchym et al. 2009; Book & Benson 2010; Tecce et al. 2010; Kimm et al. 2011; Nickerson et al. 2011).

Previous theoretical investigations of ram pressure stripping did not include all non-thermal energy components in the ISM and ICM. In general, non-thermal components include turbulent kinetic energy, magnetic fields, and cosmic-rays. Only few theoretical studies (e.g., Nulsen 1982; Otmianowska-Mazur & Vollmer 2003; Vollmer et al. 2006; Pfrommer & Dursi 2010) incorporated some of these components. First simulations of ram pressure stripping including the dynamical effects of the magnetic fields were presented in Ruszkowski et al. (2012) for late-type galaxies.

We aim to systematically investigate how non-thermal components of the ISM and ICM affect ram pressure stripping in elliptical galaxies. This is our first paper in a series of papers on this subject, and it focuses on the effect of turbu-

* E-mail: msshin@umich.edu, mateuszr@umich.edu

lent ISM on the ram pressure stripping rates, morphologies of the stripping tails, and mixing between the ISM and ICM. Although observational constraints on the turbulence properties of the hot ISM in early-type galaxies are still uncertain, there is little doubt that the hot ISM is characterised by weak turbulence and randomly oriented weak magnetic fields (Mathews & Brighenti 2003; Elmegreen & Scalo 2004; Sanders et al. 2010; Humphrey et al. 2012). Recent X-ray observations began to place meaningful constraints on the magnitude of turbulent motions in the hot gas of massive early-type galaxies, proving that the turbulence is subsonic (e.g., Churazov et al. 2008, 2010; O’grea et al. 2010; Sanders et al. 2011; de Plaa et al. 2012; Bulbul et al. 2012). Stellar winds, supernovae, and active galactic nuclei are considered to be the main energy sources for these turbulent motions (Moss & Shukurov 1996; Bregman & Parriott 2009; David et al. 2011).

We study the morphology of the ram pressure stripping tails. Sharp edges characteristic of ram pressure stripping have been detected in X-ray maps of a galaxy falling into the Fornax cluster (Machacek et al. 2005), and X-ray tails are sometimes observed in ellipticals undergoing ram pressure stripping (Randall et al. 2008; Kim et al. 2008; Machacek et al. 2006). When the strength of stripping is not significant, or the duration of the process is short, galaxies are likely to show only somewhat elongated gas distributions instead of long tails (e.g., Million et al. 2010).

In addition to the morphology of the gas distribution, ram pressure stripping also can be probed by tracking how well the ISM and ICM are mixed together for different ISM stripping rates (e.g., Schindler et al. 2005). Most previous simulations focused on how material is expelled from galaxies into the ICM. Here we also examine how much mass can be mixed into galaxies from the ICM due to the random motions of the ISM in ram pressure stripping. A direct consequence of this mixing can be a significant change of the metallicity in the galactic gas.

The organisation of the paper is as follows. We describe the simulation setup in Section 2. In Section 3, we present results of our simulations, emphasising the differences in the impact of various strengths of turbulent motions on the ram pressure stripping rates and tail morphologies. Finally, we present conclusions and discussion in Section 4.

2 SIMULATIONS

2.1 Initial conditions

Our galaxy model consists of dark matter halo and stellar mass distributions as well as the hot ISM. We assume that the gravitational field is dominated by the static distributions of the stellar and dark matter masses. Since galaxy cluster environments have strong tidal fields, we assume that the galactic gravitational field is truncated at the truncation radius $R_t = 100$ kpc. Therefore, the gas experiences no gravitation acceleration once it escapes beyond R_t . The stellar mass distribution is described by a spherical Jaffe model, while the total mass distribution follows a r^{-2} law (e.g., Ciotti et al. 2009a,b; Shin et al. 2010). Inside the effective radius of the stellar mass distribution, the mass of the dark matter halo is equal to the stellar mass. This setup

has the effective radius of 3 kpc and the total stellar mass of $\sim 10^{11} M_\odot$.

We setup the initial distribution of the ISM in hydrostatic equilibrium for the gravitational potential described above. However, this distribution is weakly perturbed by a stirring process which is explained in Section 2.3. Therefore, the precision of implementing the hydrostatic equilibrium condition is not critical in our initialisation. We note that satisfying the exact hydrostatic equilibrium condition is intrinsically difficult with finite volume methods with explicit time-stepping (Zingale et al. 2002) because gravitational acceleration acts as a sink term in the momentum equation and can cause the growth of an instability (Lian et al. 2010).

The initial ISM temperature profile has the following form

$$T(r) = \begin{cases} T_i & \text{if } r < r_i \\ 2T_0/(1 + (r/r_0)^\beta) & \text{otherwise,} \end{cases} \quad (1)$$

where $T_i = 8 \times 10^6$ K, $r_i = 50.9$ kpc, $T_0 = 1.3 \times 10^7$ K, $\beta = -3$, and $r_0 = 66.6$ kpc. The total mass of the ISM is $\sim 4.4 \times 10^{10} M_\odot$ inside R_t . The ICM is initialised with a constant density and temperature beyond R_t . The ICM temperature and density are equal to their corresponding ISM values at R_t .

We assume that ICM mean molecular weight and equation of state are same as those in the ISM. This assumption simplifies simulations by allowing us to use a single phase fluid. The temperature and density of the ICM are 2×10^7 K and 3×10^{-28} g cm $^{-3}$, respectively.

The size of the simulation box is about 1150 kpc along x -axis which is the direction of the inflowing ICM. The length of the box is about 500 kpc in both y - and z -directions. We make all zones cube-shaped by including more cells along the x -axis.

2.2 Numerical methods

We use the FLASH3 adaptive mesh refinement code with the most recent patches to solve Euler equations with gravity (Fryxell et al. 2000; Lee & Deane 2009). We employ a directionally unsplit staggered mesh hydro solver, Roe’s approximate Riemann solver with van Leer flux limiter, the ideal gas equation of state with solar metallicity, and assume the gas to be fully ionised.

We use two passive tracers – a passive fluid and passive particles. The passive advection fluid (hereafter called “colour”) is used to track the ISM mass fraction in cells. If a cell includes only the ISM, the value of this advection quantity is 1. Using this colour quantity we can measure mixing between two different materials (e.g., Shin et al. 2008). We can also determine where the mixed gas originated from by assigning different tag numbers to passive ISM and ICM particles that follow the fluid (Toschi & Bodenschatz 2009; Heath et al. 2007). We distribute 8168 particles, which correspond to the ISM, uniformly within R_t at the initial time.

We use the colour quantity as a refinement variable because we focus on resolving the mixing patterns of the ISM after it is stripped from the galaxy. Since there is no well-defined rule to choose specific refinement conditions or refinement variables (Berger & Colella 1989; Li 2010, for discussion), we adopt the standard refinement method in the

Table 1. Simulation runs

Name	ISM injection energy ($\text{cm}^2 \text{s}^{-3}$)	ISM 1D RMS velocity (Mach number)
Run 0	2.5×10^{-8}	0.022
Run 1	2.5×10^{-7}	0.038
Run 2	5.0×10^{-7}	0.048
Run 3	1.0×10^{-6}	0.067
Run 4	2.0×10^{-6}	0.093
Run 5	4.0×10^{-6}	0.119

FLASH code¹. Regions exhibiting stronger variations in the passive scalar magnitude are more finely resolved. Specifically, we use `refine_cutoff`=0.8, `derefine_cutoff`=0.2, and `refine_filter`= 10^{-2} . The refinement level outside the truncation radius is allowed to vary between 3 and 6, but it is fixed at 5 for smaller distances. The maximum spatial resolution is 1 kpc outside R_t , and 2 kpc inside this radius.

2.3 Stirring and inflow

We use a stirring module in the FLASH3 code (Eswaran & Pope 1988; Fisher et al. 2008; Ruszkowski & Oh 2010) and modify it to restrict kinetic energy injection to the region inside R_t . We investigate six different strengths of turbulent motions as shown in Table 1. The injection energies quoted in Table 1 correspond to the energy per unit mass per mode. We consider 152 driving modes, and inject energy on scales between 49 to 50 kpc (see Appendix for possible effects of the injection scales). Our random forcing scheme uses stochastic Ornstein-Uhlenbeck process and a correlation timescale of 0.01 Gyr. These parameters result in turbulent motions with mass-weighted root-mean-square 1D Mach numbers of approximately 0.022, 0.038, 0.048, 0.067, 0.093, and 0.119 for Run 0 to 5, respectively, before the onset of the ICM inflow at 0.5 Gyr.

The inflow velocity of the ICM is maintained at ~ 170 km/s, which corresponds to Mach 0.25 with respect to the ICM sound speed. Even though galaxies in groups and clusters can move faster than the speed of sound, we note that the average speed for the entire orbit can vary between subsonic and supersonic depending on properties of galaxies and clusters. Moreover, velocities of early-type galaxies are likely to be biased toward lower values than those of spiral galaxies (e.g., Adami et al. 1998; Hwang & Lee 2008). Here, we focus on the subsonic case as a simple model. If there is no obstacle, it takes about 6.6 Gyr for this flow to cross the whole simulation domain along the x -axis. All boundaries, except for the low- x (inflow) boundary, are outflow boundaries. We also test nine times higher ram pressure in Run 0 and 5 by adopting the inflow velocity of Mach 0.75. These simulations (hereafter, Run 0h and 5h) allow us find out how strongly the effects of the turbulent ISM change depending on the strength of the ram pressure.

We consider two different stirring cases. In Case A, we continuously stir the ISM with the constant injection energy

as explained above. This case corresponds to the situation when the turbulent energy sources, such as active galactic nuclei or supernova explosions, continue to operate inside the galaxies. In Case B, the turbulent energy injection is stopped after 0.5 Gyr, at which point the inflow of the ICM begins. All simulations run up to 6 Gyr.

3 RESULTS

We performed twelve simulations for six different strengths and two different durations of the turbulent energy injection, that is, Cases A and B. We also simulated four strong ram pressure stripping cases for two strengths of turbulence driving in Case A and B. We now present the results of these simulations, focusing on relative differences among the runs.

3.1 Overall evolution

Figure 1 shows the time sequence of the evolution of the ISM in a galaxy that is subject to the ram pressure stripping. Left column corresponds to Run 1 and right one to Run 4. Run 0 corresponds to extremely weak stirring and can be thought of as a reference non-turbulent case. Both columns are for Case A, where the stirring energy is continuously supplied to the ISM. From top to bottom, each row corresponds to 0.75, 2, 4, and 6 Gyr. This figure demonstrates that the turbulence is well developed before the ICM wind begins to interact with the galaxy. The ram pressure produces a long turbulent tail, and the tail properties vary with the strength of the ISM turbulence. In particular, Run 1 reveals a more discontinuous tail than Run 4. This difference becomes more evident at later times. Moreover, Run 4 corresponds to a longer and broader tail than Run 1. This is due to the fact that the stripping from the outer ISM layers is enhanced in Run 4. We quantify these morphological differences in the following subsection.

3.2 Tail morphology

In order to quantify the evolution of the spatial distribution of the ISM, we use colour weighting (see above). The colour quantity C represents the ISM fraction in cells, and we use it to obtain the mass of the ISM in each cell. We then employ the following equations to describe the evolution of the tail properties

$$\langle x_{\text{ISM}} \rangle = \frac{\sum_i C_i \rho_i V_i x_i}{\sum_i C_i \rho_i V_i}, \quad (2)$$

$$\delta x_{\text{ISM}} = \sqrt{\frac{\sum_i C_i \rho_i V_i (x_i - \langle x_{\text{ISM}} \rangle)^2}{\sum_i C_i \rho_i V_i}}, \quad (3)$$

where the index i represents cell number, and ρ , V , and x , correspond to density, cell volume, and cell x -coordinates, respectively. The quantity $\langle x_{\text{ISM}} \rangle$ traces the overall shift of the ISM mass after it is stripped from the galaxy. Finally, δx_{ISM} , and its y -direction counterpart δy_{ISM} , quantify the widths the distributions of the ISM along the x and y axes.

Figure 2 shows the evolution of $\langle x_{\text{ISM}} \rangle$, δx_{ISM} , and δy_{ISM} . These measurements quantify what is shown in Figure 1. When the stirring process is continuous (Case A; left

¹ http://www.asci.uchicago.edu/site/flashcode/user_support/flash3 Ug_3p3/node14.html#SECTION05163000000000000000

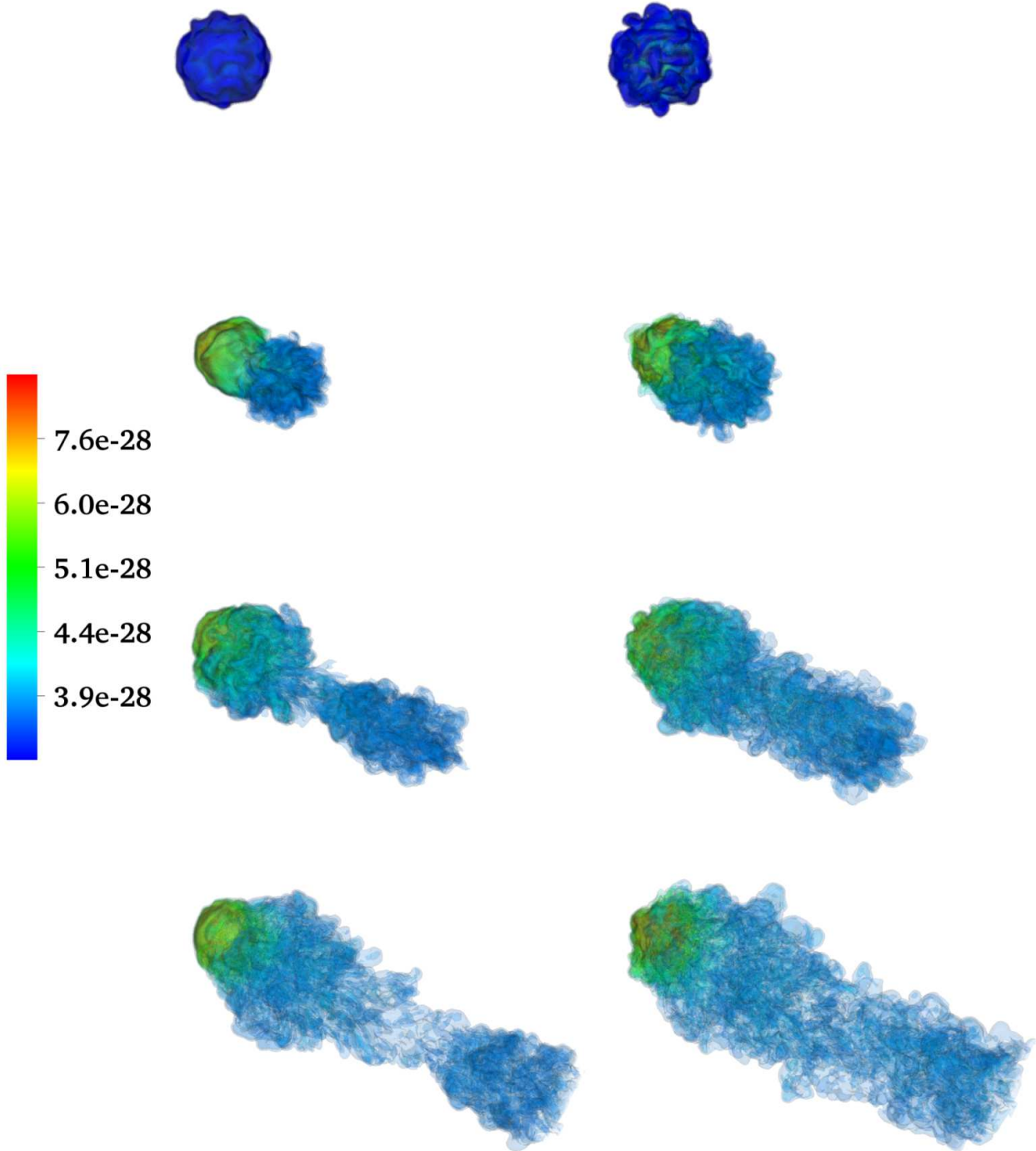


Figure 1. ISM density distributions for ten isosurfaces of the ISM mass fractions ranging linearly from 0.01 to 1. The unit of density is g cm^{-3} . Runs 1 and 4 for Case A are shown in the left and right columns, respectively. From top to bottom, each row corresponds to 0.75, 2, 4, and 6 Gyr. Because the top two panels show the early phase, the radius of the approximately spherical ISM distribution is close to $R_t = 100$ kpc.

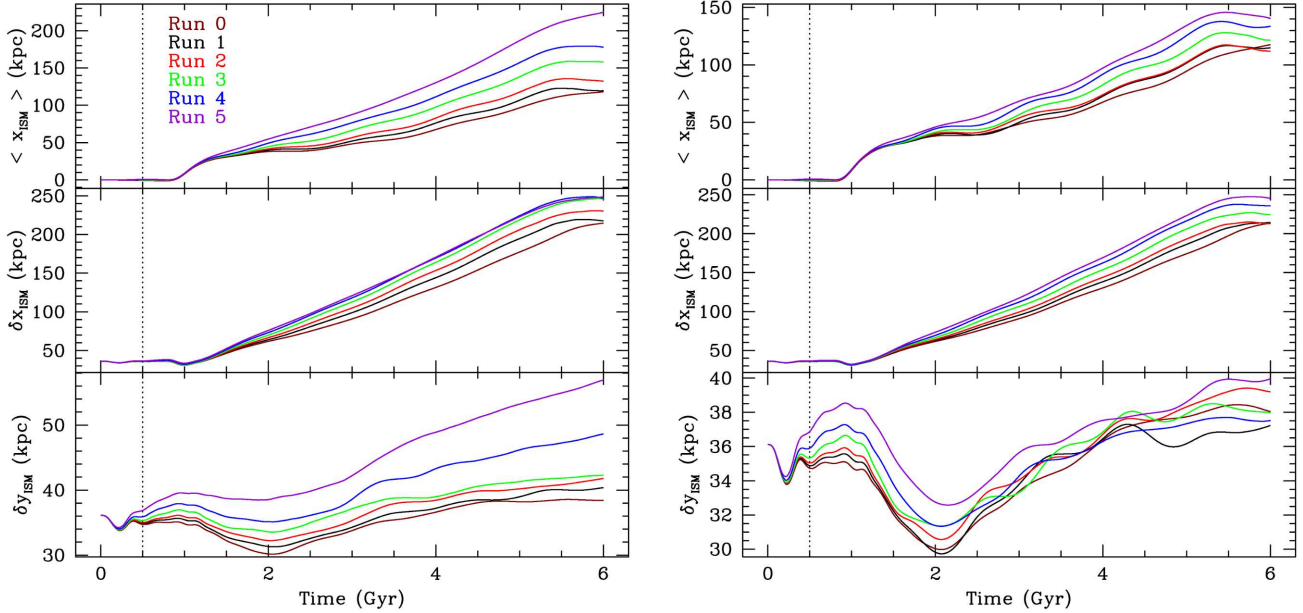


Figure 2. Evolution of $\langle x_{\text{ISM}} \rangle$, δx_{ISM} , and δy_{ISM} . The simulations with the continuous supply of the turbulent energy (*left*; Case A) lead to larger differences in $\langle x_{\text{ISM}} \rangle$ among the runs than those without the continuous energy supply (*right*; Case B). The same tendency is found in the distributions of δx_{ISM} and δy_{ISM} .

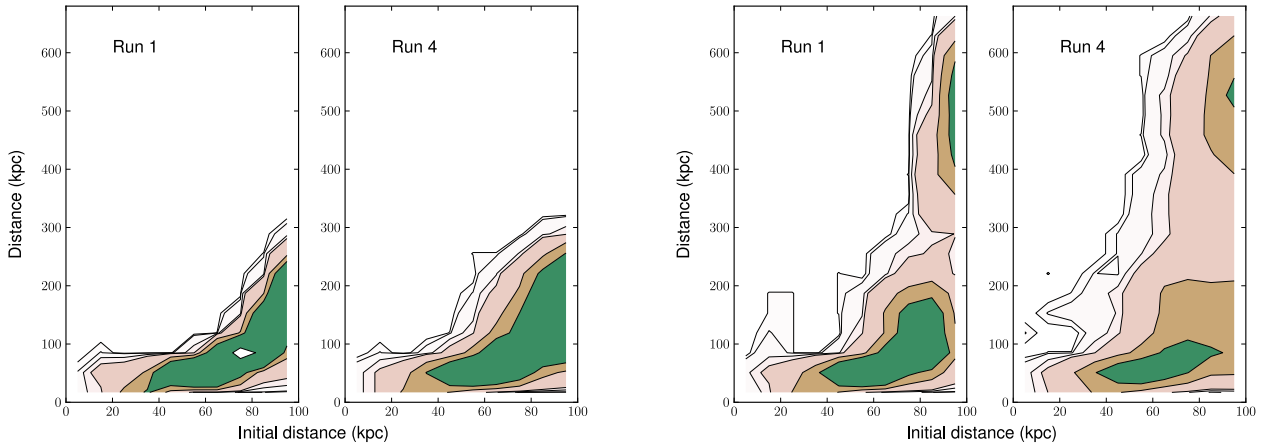


Figure 3. Density distributions of the passively moving particles in Runs 1 and 4 at 2 (*left*) and 4.5 (*right*) Gyr. The number density of the passive particles is measured on uniform grids with bin sizes of 10 and 34 kpc for horizontal and vertical axes, respectively. The contour lines correspond to the number densities 5×10^{-5} , 1×10^{-4} , 5×10^{-4} , 1×10^{-3} , 5×10^{-3} , 1×10^{-2} , and $4 \times 10^{-2} \text{ kpc}^{-2}$. All plots show the distributions corresponding to Case A.

panel), Run 4 creates a longer tail than Run 1, and this difference increases with time up to 60 kpc at 6 Gyr. However, the difference is much smaller in Case B runs (right panel). This comparison also confirms that the initial expansion of the ISM caused by the injected energy from the stirring process is not the cause for the difference between Runs 1 and 4 in Case A. If the initial expansion was the main reason for the differences among different runs in Case A, the same effect should be found in Case B too. Yet, in the absence of the continuous stirring (Case A), no significant differences are seen among different runs. Therefore,

the continuous supply of the turbulent energy causes differences found between Cases A and B.

Figure 2 shows that stronger turbulence in Case A results in wider dispersions of the ISM parallel and perpendicular to the direction of the ram pressure. Even though in Case B the energy is not supplied continuously to the ISM, the evolution of δx_{ISM} is similar to what we find in Case A. We do not find a significant effect of turbulence on δy_{ISM} in Case B. Although Case B does not exhibit significant deviations among different runs, general trends in the tail evolution Case B is the same as in Case A. In partic-

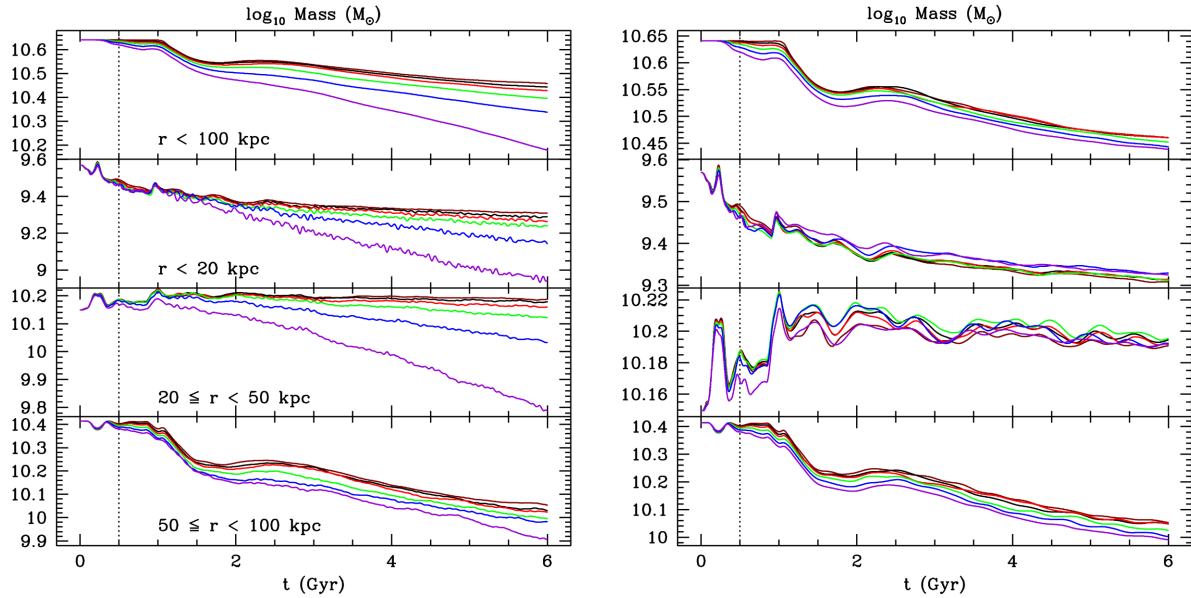


Figure 4. Mass evolution of the intrinsic ISM for Case A (*left*) and Case B (*right*). From top to bottom, each panel shows the mass in four different radial zones: $r < 100$ kpc, $r < 20$ kpc, $20 \text{ kpc} \leq r < 50$ kpc, and $50 \text{ kpc} \leq r < 100$ kpc ($R_t = 100$ kpc). The dotted line corresponds to 0.5 Gyr when the inflow of the ICM starts to enter the simulation box. The colour coding of the different lines is the same as in Figure 2. We note that the ranges of the vertical axes are not same in the left and right columns.

Table 2. Times corresponding to the removal of 10%, 20%, and 30% of the ISM in Case A (measured from the onset of the ICM inflow at 0.5 Gyr).

Name	Δt_{10} (Gyr)	Δt_{20} (Gyr)	Δt_{30} (Gyr)
Run 0	0.746	2.314	4.010
Run 1	0.729	1.192	3.721
Run 2	0.709	1.079	3.433
Run 3	0.672	0.977	2.815
Run 4	0.619	0.896	2.132
Run 5	0.546	0.789	1.242

ular, at around 2 Gyr, the initial stripping generates short and narrow tail immediately behind the galaxy (see Figure 1). This is due to a converging ICM flow behind the galaxy. This narrowing is a transient feature and the tail widens after 2 Gyr.

3.3 Origin of the ISM in the tails

The origin of the ISM stripped away from the galaxy can be used to understand what kind of materials are transported to the ICM by the ram pressure stripping. As explained in the previous section, we map the initial positions of the particles to their temporal positions. This allows us to check where exactly the stripped material in the tail came from.

Figure 3 shows the distributions of particle surface densities in the two-dimensional space defined by the initial and current particle positions measured with respect to the galactic centre. Left panel corresponds to 2 Gyr and the right one to 4.5 Gyr. Initially, all particles were distributed uniformly inside the truncation radius.

The results presented in Figure 3 allow us to make to

points. First, most of the stripped gas originates from the outer parts of the galaxy near the truncation radius, and, second, higher turbulence levels enable gas removal from deeper layers of the galactic atmosphere. Regarding the first point, the gas originally located near the truncation radius is always transported to largest radii, independently of the turbulence level. Regarding the second point, a significant amount of the ISM initially residing between 60 and 80 kpc is stripped beyond 200 kpc at 2 Gyr in Run 4. This makes the distribution of the particle density in Run 4 appear wider at a given distance beyond 200 kpc than in Run 1. This is again because more vigorous ISM turbulence in Run 4 more efficiently transports the ISM from small radii to the ISM-ICM interface from which the gas is permanently removed.

Figure 3 also shows that the narrow part of the tail found in Run 1 (see Figure 1) is caused by inefficient stripping of the ISM. At 4.5 Gyr, Run 1 has fewer particles at ~ 300 kpc than Run 4, which leads to narrower tail. This low-density structure of the tail is caused by the inefficient stripping of the ISM that initially resided at radii larger than 60 kpc.

3.4 Evolution of the ISM mass retained in the galaxy

Since we use the passive scalar quantity to identify ISM and ICM separately, we can follow the evolution of the gas that originally belonged to the ISM. Figure 4 shows the evolution of the ISM mass in four different radial bins inside R_t . We find significant differences between Case A and B. A continuous supply of the turbulent energy enhances internal mixing of the ISM, resulting in the increase in the net mass loss rate of the ISM. This effect is not seen in Case B.

We find that the strength of turbulence has a noticeable

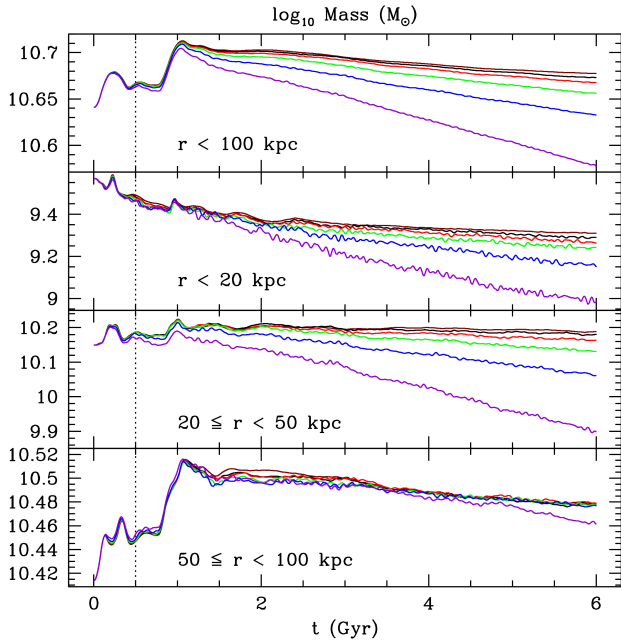


Figure 5. Evolution of the total gas mass inside $R_t = 100$ kpc for Case A. From top to bottom, each panel shows the mass in four different radial zones: $r < 100$ kpc, $r < 20$ kpc, $20 \text{ kpc} \leq r < 50$ kpc, and $50 \text{ kpc} \leq r < 100$ kpc. The dotted line corresponds to 0.5 Gyr when the inflow of the ICM starts to enter the simulation box. The colour coding of the different lines is the same as in Figure 2.

effect on the distribution of the intrinsic ISM inside R_t in Case A. As shown in Figure 4, in Case A at 6 Gyr, Run 0 retains about $2.87 \times 10^{10} M_\odot$ of the intrinsic ISM, while Run 5 has about $1.51 \times 10^{10} M_\odot$, i.e. about 2 times less. 2 summarises time scales of 10, 20, and 30% ISM mass loss after the inflow of ICM produces ram pressure in Case A. In Case B, although we find the same general trend as Case A, the difference is smaller.

This evolution of the intrinsic ISM mass hints at the possibility that, in Case A, a significant amount of the inflowing ICM penetrates the galaxy and mixes with the ISM. The volume initially occupied by the intrinsic ISM can be partially refilled by the inflowing ICM if the ISM-ICM mixing is efficient within R_t .

3.5 Evolution of the total gas mass inside the galaxy

In Figure 5, we show the evolution of the total gas mass including both the ISM and ICM inside R_t . We find that the ICM temporarily accumulates mainly over $50 \leq r < 100$ kpc in Case A. The total mass of the gas increases up to $\sim 3.3 \times 10^{10} M_\odot$ over $50 \leq r < 100$ kpc as the ICM compresses the ISM and then blends with the ISM. However, the ICM caught in the galaxy is finally expelled after ~ 1 Gyr by the combined action of the ram pressure stripping and continuous supply of turbulent energy.

As shown in Figure 4, the mass of the intrinsic ISM does not depend sensitively on the level of turbulence in Case B. Similarly, for the total gas mass within R_t , we do

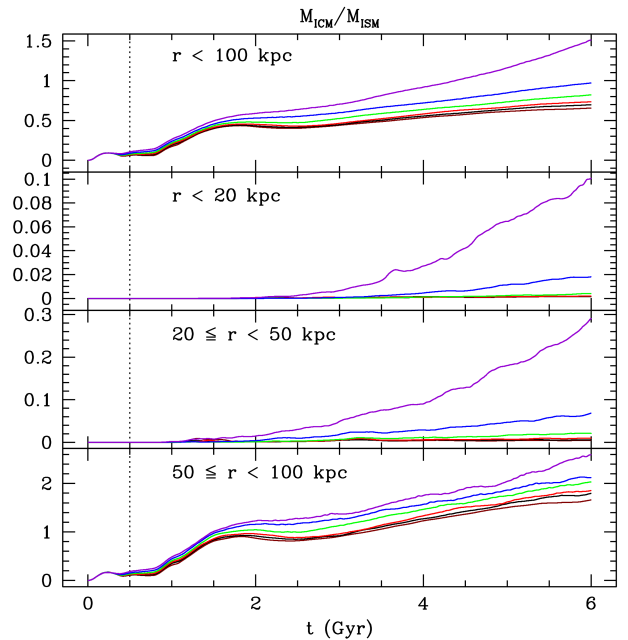


Figure 6. Evolution of the ratio of the intrinsic ICM mass over the intrinsic ISM mass inside R_t for Case A. The colour scheme is the same as in Figure 2.

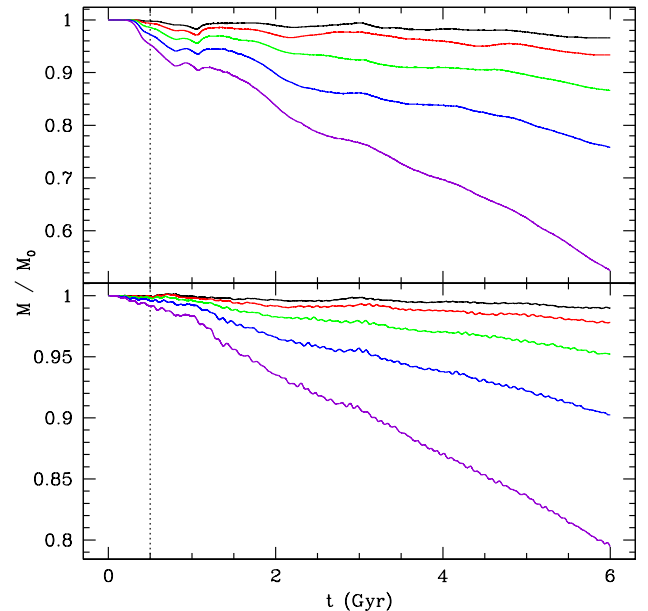


Figure 7. Evolution of the intrinsic ISM mass (*top*) and the total gas mass (*bottom*) inside R_t with respect to masses for Run 0 in Case A. The colour scheme is the same as in Figure 2.

not observe strong trends with the turbulence strength in Case B, and therefore we do not show Case B in Figure 5. However, overall evolution of the total mass as a function of radius in Case B is similar to that in Case A.

The fractional change in the total gas mass within R_t is smaller than the fractional change in the intrinsic ISM

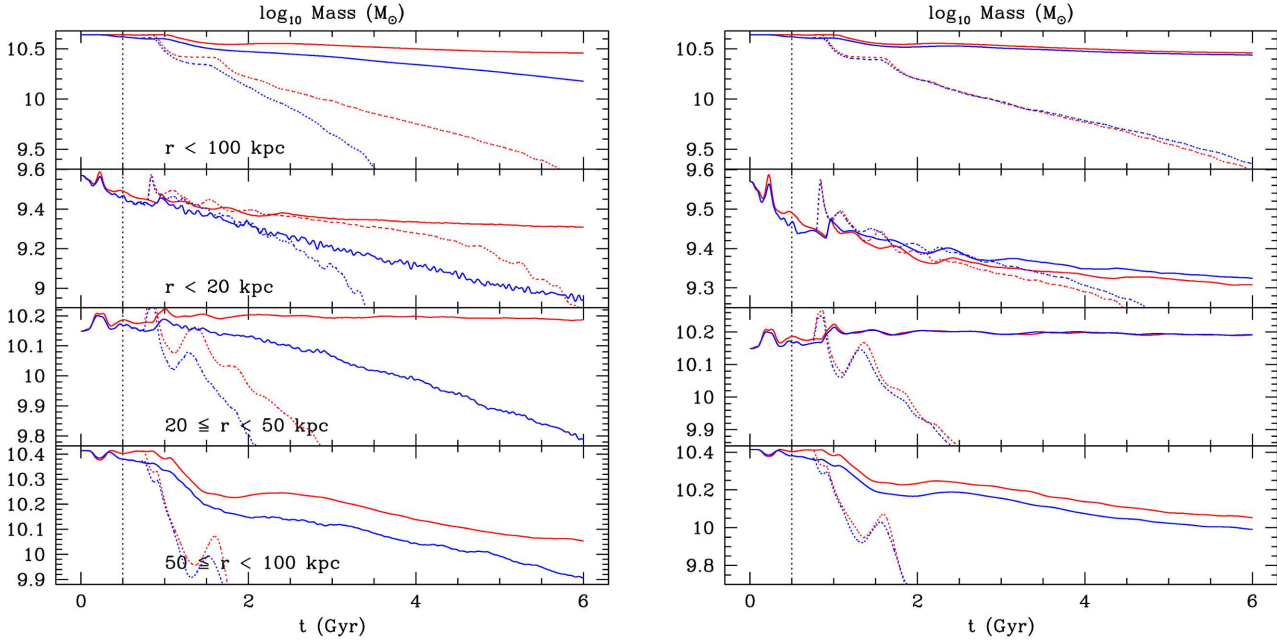


Figure 8. Mass evolution of the intrinsic ISM for Case A (left) and Case B (right) in Run 0 (red) and 5 (blue) for the low (solid line) and high (dotted line) ram pressure stripping. From top to bottom, each panel shows the mass in four different radial zones: $r < 100$ kpc, $r < 20$ kpc, $20 \text{ kpc} \leq r < 50$ kpc, and $50 \text{ kpc} \leq r < 100$ kpc ($R_t = 100$ kpc). The dotted vertical line corresponds to 0.5 Gyr when the inflow of the ICM starts to enter the simulation box. We note that the range of the vertical axis are not same in the left and right columns for the panel of $20 \text{ kpc} \leq r < 50$ kpc.

retained within R_t (c.f. top panel in Figure 5 and top left panel in Figure 4, respectively). This suggests that the ICM mixes with the intrinsic ISM.

Figure 6 summarises how much mass is contributed by the ICM and ISM inside R_t as a function of time for Case A. As the strength of the turbulent motions in the ISM increases, the fraction of the ICM penetrating into the galaxy increases, resulting in about 1.5 times more ICM mass than the ISM mass inside R_t in Run 5 at 6 Gyr. Considering only the outer region of the galaxy over $50 \leq r < 100$ kpc, this fraction is about 2.6 in Run 5 while it becomes about 1.6 in Run 0.

Figure 7 presents the relative differences in the mass loss caused by different strengths of the ISM turbulence. At 6 Gyr, Run 5 retains almost twice less ISM than Run 0, which corresponds to weak ISM turbulence. Yet, considering the total mass including ISM and ICM inside R_t , Run 5 has only 20% less mass than Run 0, because more ICM is blended with the ISM in Run 5 than in Run 0. Importantly, the differences among different runs show strongly non-linear dependence on the ISM velocity dispersion. In Run 4, the intrinsic ISM mass is about 25% less than in Run 0 at 6 Gyr, while twice less intrinsic ISM is retained in Run 5 than in Run 0.

3.6 Ram pressure stripping for higher ICM inflow velocity

By comparing results from Run 0 and 5 to those from Run 0h and 5h, we investigate how the increasing strength of the ram pressure alters the effects of the turbulent ISM on the stripping efficiency. Figure 8 shows that the increased ram

pressure of the ICM enhances stripping in both Runs 0 and 5. Because the ram pressure is nine times stronger in Run 0h than in Run 0, the mass of the ISM left inside the galaxy is much lower in Run 0h than in Run 0. Similarly, Run 5h retains ~ 13 times less gas than Run 5 at ~ 3.5 Gyr. The increased inflow speed significantly increases the efficiency of the initial stripping in the outer $50 \text{ kpc} \leq r < 100$ kpc region. As the stripping process continues, some amount of the ISM originally located at the centre of the galaxy (i.e., $r < 20$ kpc) is moved to the outer regions gradually by the turbulent ISM, and then is stripped from the galaxy. Therefore, the increase in the stripping efficiency is larger in Run 5h than 0h. For example, top left panel in Figure 8 shows that Run 0h retains ~ 3 times more intrinsic ISM at ~ 3 Gyr since the onset of stripping than Run 5h.

Comparison of Cases A and B in Figure 8, shows that continuous supply of the turbulence energy amplifies the efficiency of ram pressure stripping. In Run 5h, Case A keeps about 4 times less ISM than Case B at around 3.5 Gyr. The difference between Case A and B is particularly striking in the central regions ($r < 20$ kpc). We note that we continuously supply the turbulence energy in Case A even after the substantial amount of the ISM is stripped at around 2 Gyr. This might not be a realistic assumption for turbulence driven by stellar and/or AGN processes. After the large amount of the cold ISM has been removed from a galaxy, the galaxy may not be able to generate strong turbulence due to processes such as star formation, supernova explosions, and AGN feedback. Consequently, the strong ram pressure stripping results beyond ~ 3 Gyr may not be reliable. However, we argue that these cases serve to bracket the range of possible solutions.

4 DISCUSSION AND CONCLUSIONS

We show that the continuous supply of small to moderate amount of turbulent kinetic energy to the ISM enhances the ISM mass loss rate in elliptical galaxies experiencing ram pressure stripping, and increases the penetration of the ICM into the galaxies (see Figure 7). The spatial distribution of the stripped ISM can be wider and more extended along the direction of galaxy motion (see Figures 1, 2, and 3), when AGN feedback and/or stellar processes such as star formation are present. Our results imply that early-type galaxies characterised by the turbulent ISM should efficiently disperse their ISM throughout galaxy clusters.

The origin of the stripped ISM in the tails shows that the ram pressure stripping with the turbulent motions in the ISM boosts the mixing between the central region and the outer region of the galaxy. This implies that the distributions of gas properties in the tails can be used to infer the distribution of the intrinsic ISM properties such as gas metallicity inside galaxies. Since the distant part of the tail in Run 5 is more mixed with the central gas inside the galaxy than in Run 0, we expect that the properties of the stripped ISM should show weaker gradients of the gas properties along the tail in Run 5 than in Run 0.

For example, there might be a gradient in metallicity distribution along the ram pressure stripping tail. In general, the ISM in the central regions of early-type galaxies is more metal-rich than in the outer regions (e.g., Million et al. 2011; Humphrey et al. 2011). Therefore, very low levels of the ISM turbulence in early-type galaxies make the stripping tail have only low metallicity ISM along the tail, contributing negligibly to the ICM metal enrichment (see, Schindler & Diaferio 2008; Kim et al. 2008, for discussion of the ICM enrichment efficiency). However, we note that this depends on the initial metallicity distribution in the galaxy. If a galaxy has a shallow metallicity gradient before experiencing ram pressure stripping, it can flatten the metallicity distribution along the tail and lead to more significant ICM enrichment even when the strength of the ISM turbulence is weaker.

The evolution of the mass inside the galaxy implies that a significant fraction of the gas mass measured in observations can be explained by the ICM gas that got temporarily incorporated into the ISM. As Figure 6 shows, galaxies with the strong turbulent motions in the ISM easily blend the inflowing ICM with the ISM. Therefore, the properties of the hot X-ray emitting ISM in the galaxy experiencing ram pressure stripping might have been altered by the inflowing ICM, in particular, in the outer regions.

For example, the metallicity of the ICM in low-redshift galaxy clusters is about $0.5 Z_{\odot}$ (Anderson et al. 2009) and can be much lower than that of the ISM (Humphrey & Buote 2006; Ji et al. 2009). Thus, mixing of the ICM with galactic gas can alter the metallicity of the ISM and the metallicity gradient inside cluster galaxies. This contamination can be particularly significant in the outer regions of galaxies when the ISM is turbulent. Interestingly, if the galaxy has an initially flat metallicity profile at the level of $2 Z_{\odot}$, and if the metallicity of the ICM is about $0.5 Z_{\odot}$, then the ram pressure stripping will lower the mass-weighted metallicity to around 0.9 and $1.9 Z_{\odot}$ in $50 \leq r < 100$ kpc and $r < 20$ kpc, respectively (with the mass ratios shown in Figure 6 for

Run 5 at 6 Gyr) This specific case illustrates how ram pressure stripping in the presence of turbulent ISM can steepen ISM metallicity profiles. This steepening effect is expected to be more pronounced as the strength of ISM turbulence increases.

The models presented here allow one to study the effects of turbulence on the ram pressure stripping process via a conceptually simple approach. The advantage of this approach lies in providing a clear intuitive picture of how the turbulent ISM affects the gas stripping. These models form a framework for future studies that will relax some of the assumptions made in the present work.

Our current simulations do not include a few important physical processes that are required to make detailed observational predictions for the ram pressure stripping process. First, we do not include radiative cooling processes (see, Kaastra et al. 2008, for a review), which will lead to the formation of dense cold gas clouds (e.g., Sun et al. 2007; Sivanandam et al. 2010; Yirak et al. 2010). Second, self-gravity of the gas is not included. Self-gravity can alter the evolution of the stripped ISM by accelerating the collapse of these dense cold gas clouds. Third, the spatial resolution of our simulations is not high enough to fully cover an extremely broad inertial range of the turbulent ISM (see Moin & Mahesh 1998; Brandenburg & Nordlund 2011, for a review). Fourth, we have neglected magnetic fields, which may affect the efficiency of mixing of the ISM and ICM, suppress viscosity and thermal conduction between the stripping tail of the cold gas and the hot ICM, and introduce non-trivial dynamical effects. Finally, the energy sources of the turbulence in our simulations are not directly controlled by the relevant astrophysical processes such as star formation and AGN. Continuous mass loss by ram pressure stripping can affect star formation and AGN feedback (Babul & Rees 1992; Murakami & Babul 1999; Kronberger et al. 2008; Shin et al. 2012), increasing or decreasing energy injected to the turbulent ISM.

Our main concern is the fact that our model currently does not take into account a possible coupling between the efficiency of stirring of the gas by star formation and AGN and the efficiency of stripping. For example, it is conceivable that enhanced stellar or AGN feedback could increase the level of turbulence, accelerate the mass removal from the galaxy, and thus reduce the fuel supply for these feedback processes and the efficiency of the ram pressure stripping process. Consequently, less gas would be available to fuel AGN and star formation, and the stirring efficiency would slow down. Our model currently does not incorporate such mechanism. However, we show that the efficiency of ram pressure stripping depends sensitively on the duration of stirring, and our models for the continuous (Case A) and initial (Case B) stirring likely bracket the range of possibilities.

In future work, we will relax some of the assumptions and simplifications made here. The second paper in this series will investigate the effect of weakly magnetised turbulent ISM in elliptical galaxies on the ram pressure stripping process.

ACKNOWLEDGEMENTS

We are grateful to Karen Yang and Dongwook Lee for useful discussions. We thank the referee (Eugene Churazov) for his valuable comments that improved this manuscript. MR acknowledges NSF grant 1008454. This work used the Extreme Science and Engineering Discovery Environment (XSEDE), which is supported by National Science Foundation grant number OCI-1053575. The software used in this work was in part developed by the DOE NNSA-ASC OASCR Flash Center at the University of Chicago.

REFERENCES

- Adami C., Biviano A., Mazure A., 1998, *A&A*, 331, 439
 Anderson M. E., Bregman J. N., Butler S. C., Mullis C. R., 2009, *ApJ*, 698, 317
 Babul A., Rees M. J., 1992, *MNRAS*, 255, 346
 Balsara D., Livio M., O’Dea C. P., 1994, *ApJ*, 437, 83
 Berger M. J., Colella P., 1989, *Journal of Computational Physics*, 82, 64
 Book L. G., Benson A. J., 2010, *ApJ*, 716, 810
 Brandenburg A., Nordlund Å., 2011, *Reports on Progress in Physics*, 74, 046901
 Bregman J. N., Parriott J. R., 2009, *ApJ*, 699, 923
 Bulbul G. E., Smith R. K., Foster A., Cottam J., Loewenstein M., Mushotzky R., Shafer R., 2012, *ApJ*, 747, 32
 Churazov E., Forman W., Vikhlinin A., Tremaine S., Gerhard O., Jones C., 2008, *MNRAS*, 388, 1062
 Churazov E., Tremaine S., Forman W., Gerhard O., Das P., Vikhlinin A., Jones C., Böhringer H., Gebhardt K., 2010, *MNRAS*, 404, 1165
 Ciotti L., Morganti L., de Zeeuw P. T., 2009a, *MNRAS*, 393, 491
 Ciotti L., Ostriker J. P., Proga D., 2009b, *ApJ*, 699, 89
 David L. P., O’Sullivan E., Jones C., Giacintucci S., Vrtilke J., Raychaudhury S., Nulsen P. E. J., Forman W., Sun M., Donahue M., 2011, *ApJ*, 728, 162
 de Plaa J., Zhuravleva I., Werner N., Kaastra J. S., Churazov E., Smith R. K., Raassen A. J. J., Grange Y. G., 2012, *A&A*, 539, A34
 Domainko W., Mair M., Kapferer W., van Kampen E., Kronberger T., Schindler S., Kimeswenger S., Ruffert M., Mangete O. E., 2006, *A&A*, 452, 795
 Elmegreen B. G., Scalo J., 2004, *ARA&A*, 42, 211
 Eswaran V., Pope S. B., 1988, *Computers and Fluids*, 16, 257
 Fisher R. T., Kadanoff L. P., Lamb D. Q., Dubey A., Plewa T., Calder A., Cattaneo F., Constantin P., Foster I. T., Papka M. E., Abarzhi S. I., Asida S. M., Rich P. M., Glendenin C. C., Antypas K., Sheeler D. J., Reid L. B., Gallagher B., Needham S. G., 2008, *IBM Journal of Research and Development*, 52, 127
 Fryxell B., Olson K., Ricker P., Timmes F. X., Zingale M., Lamb D. Q., MacNeice P., Rosner R., Truran J. W., Tufo H., 2000, *ApJS*, 131, 273
 Gunn J. E., Gott III J. R., 1972, *ApJ*, 176, 1
 Heath D., Krause M., Alexander P., 2007, *MNRAS*, 374, 787
 Hester J. A., 2006, *ApJ*, 647, 910
 Humphrey P. J., Buote D. A., 2006, *ApJ*, 639, 136
 Humphrey P. J., Buote D. A., Brighenti F., Gebhardt K., Mathews W. G., 2012, *ArXiv e-prints/1205.0256*
 Humphrey P. J., Buote D. A., Canizares C. R., Fabian A. C., Miller J. M., 2011, *ApJ*, 729, 53
 Hwang H. S., Lee M. G., 2008, *ApJ*, 676, 218
 Jáchym P., Köppen J., Palouš J., Combes F., 2009, *A&A*, 500, 693
 Ji J., Irwin J. A., Athey A., Bregman J. N., Lloyd-Davies E. J., 2009, *ApJ*, 696, 2252
 Kaastra J. S., Paerels F. B. S., Durret F., Schindler S., Richter P., 2008, *Space Sci. Rev.*, 134, 155
 Kapferer W., Kronberger T., Ferrari C., Riser T., Schindler S., 2008, *MNRAS*, 389, 1405
 Kapferer W., Sluka C., Schindler S., Ferrari C., Ziegler B., 2009, *A&A*, 499, 87
 Kim D.-W., Kim E., Fabbiano G., Trinchieri G., 2008, *ApJ*, 688, 931
 Kimm T., Yi S. K., Khochfar S., 2011, *ApJ*, 729, 11
 Kronberger T., Kapferer W., Ferrari C., Unterguggenberger S., Schindler S., 2008, *A&A*, 481, 337
 Lee D., Deane A. E., 2009, *Journal of Computational Physics*, 228, 952
 Li S., 2010, *Journal of Computational and Applied Mathematics*, 233, 3139
 Lian C., Xia G., Merkle C. L., 2010, *Computers & Fluids*, 39, 1909
 Machacek M., Dosaj A., Forman W., Jones C., Markevitch M., Vikhlinin A., Warmflash A., Kraft R., 2005, *ApJ*, 621, 663
 Machacek M., Jones C., Forman W. R., Nulsen P., 2006, *ApJ*, 644, 155
 Mathews W. G., Brighenti F., 2003, *ARA&A*, 41, 191
 Mayer L., Mastropietro C., Wadsley J., Stadel J., Moore B., 2006, *MNRAS*, 369, 1021
 McCarthy I. G., Frenk C. S., Font A. S., Lacey C. G., Bower R. G., Mitchell N. L., Balogh M. L., Theuns T., 2008, *MNRAS*, 383, 593
 Million E. T., Allen S. W., Werner N., Taylor G. B., 2010, *MNRAS*, 405, 1624
 Million E. T., Werner N., Simionescu A., Allen S. W., 2011, *MNRAS*, 418, 2744
 Moin P., Mahesh K., 1998, *Annual Review of Fluid Mechanics*, 30, 539
 Moss D., Shukurov A., 1996, *MNRAS*, 279, 229
 Murakami I., Babul A., 1999, *MNRAS*, 309, 161
 Nickerson S., Stinson G., Couchman H. M. P., Bailin J., Wadsley J., 2011, *MNRAS*, 415, 257
 Nulsen P. E. J., 1982, *MNRAS*, 198, 1007
 Ogrea G. A., Hatch N. A., Simionescu A., Böhringer H., Brüggem M., Fabian A. C., Werner N., 2010, *MNRAS*, 406, 354
 Otmianowska-Mazur K., Vollmer B., 2003, *A&A*, 402, 879
 Pfrommer C., Dursi J. L., 2010, *Nature Physics*, 6, 520
 Randall S., Nulsen P., Forman W. R., Jones C., Machacek M., Murray S. S., Maughan B., 2008, *ApJ*, 688, 208
 Roediger E., Brüggem M., 2007, *MNRAS*, 380, 1399
 Roediger E., Brüggem M., 2008, *MNRAS*, 388, L89
 Ruszkowski M., Brüggem M., Lee D., Shin M.-S., 2012, *ArXiv e-prints/1203.1343*
 Ruszkowski M., Oh S. P., 2010, *ApJ*, 713, 1332
 Sanders J. S., Fabian A. C., Smith R. K., 2011, *MNRAS*, 410, 1797

- Sanders J. S., Fabian A. C., Smith R. K., Peterson J. R., 2010, MNRAS, 402, L11
- Schindler S., Diaferio A., 2008, Space Sci. Rev., 134, 363
- Schindler S., Kapferer W., Domainko W., Mair M., van Kampen E., Kronberger T., Kimeswenger S., Ruffert M., Mangete O., Breitschwerdt D., 2005, A&A, 435, L25
- Shin M.-S., Ostriker J. P., Ciotti L., 2010, ApJ, 711, 268
- Shin M.-S., Ostriker J. P., Ciotti L., 2012, ApJ, 745, 13
- Shin M.-S., Stone J. M., Snyder G. F., 2008, ApJ, 680, 336
- Sivanandam S., Rieke M. J., Rieke G. H., 2010, ApJ, 717, 147
- Sun M., Donahue M., Voit G. M., 2007, ApJ, 671, 190
- Tecce T. E., Cora S. A., Tissera P. B., Abadi M. G., Lagos C. D. P., 2010, MNRAS, 408, 2008
- Tonnesen S., Bryan G. L., 2008, ApJ, 684, L9
- Tonnesen S., Bryan G. L., van Gorkom J. H., 2007, ApJ, 671, 1434
- Toschi F., Bodenschatz E., 2009, Annual Review of Fluid Mechanics, 41, 375
- Vollmer B., Soida M., Otmianowska-Mazur K., Kenney J. D. P., van Gorkom J. H., Beck R., 2006, A&A, 453, 883
- Yirak K., Frank A., Cunningham A. J., 2010, ApJ, 722, 412
- Zingale M., Dursi L. J., ZuHone J., Calder A. C., Fryxell B., Plewa T., Truran J. W., Caceres A., Olson K., Ricker P. M., Riley K., Rosner R., Siegel A., Timmes F. X., Vladimirova N., 2002, ApJS, 143, 539

APPENDIX A: EFFECT OF TURBULENCE DRIVING SCALES

The properties of the ISM turbulence can affect the stripping efficiency. In particular, the stripping efficiency can depend on the outer turbulence driving scale l_{turb} . This is expected because the effective diffusion coefficient $\sim l_{turb} v_{turb}$, where v_{turb} is a characteristic turbulence velocity. In order to investigate this dependence, we perform an additional simulation which corresponds to Run 5 for Case A, but where the outer turbulence scale is reduced from ~ 50 kpc to ~ 25 kpc, and where the energy injection rate per mode is adjusted such that the total amount of the turbulent energy injection within R_t is the same as in the original Run 5 for Case A.

As shown in Figures A1 and A2, the new simulation shows less stripping and weaker mixing between the ICM and ISM than in the original Run 5. The mass-weighted root-mean-square 1D Mach number of the ISM in the new simulation is about 0.1 which is almost the same as in the original Run 5. This Mach number corresponds to the state of the ISM before the onset of the ICM inflow. Since the energy injection rate is unchanged, and thermal energy dominates over the time-integrated dissipation rate of the injected energy, the Mach number does not change significantly. Since the new simulation lacks large-scale motions in the ISM, the diffusion of the ISM with the ICM becomes inefficient. At 6 Gyr, about 20% larger amount of the ISM survives stripping in the new simulation than in the original Run 5. Figure A2 shows that the suppression of gas stripping is relatively strong at intermediate radii. Specifically,

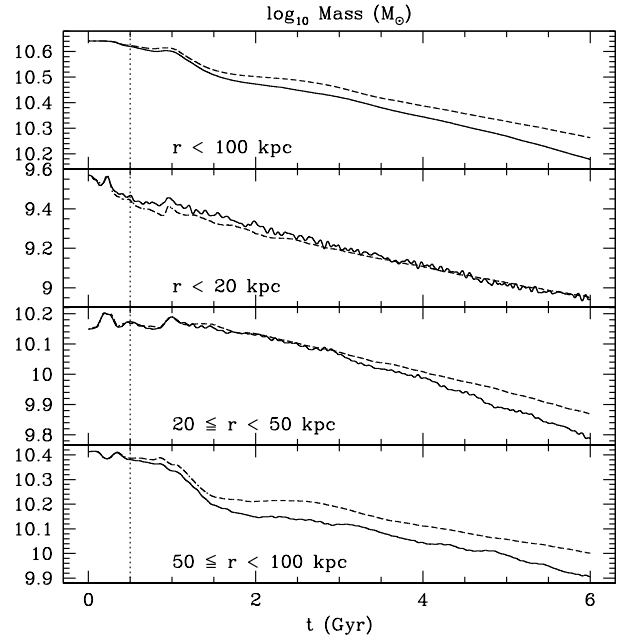


Figure A1. Evolution of the intrinsic ISM mass for Run 5 with smaller turbulent driving scale (*dashed line*) in Case A, compared to the original run (*solid line*). The dotted line corresponds to 0.5 Gyr when the inflow of the ICM starts to enter the simulation box.

for $20 \leq r < 50$ kpc, two times less ISM is retained in this shell at 6 Gyr.

Figure A3 shows the ICM density distribution in a plane centred on the galaxy and parallel to the direction of the ICM inflow. Comparison of the panels in the same columns demonstrates that mixing is reduced in the new simulation: the area occupied by lower density gas is larger, and the penetration of the ICM deeper into the galactic potential is suppressed.

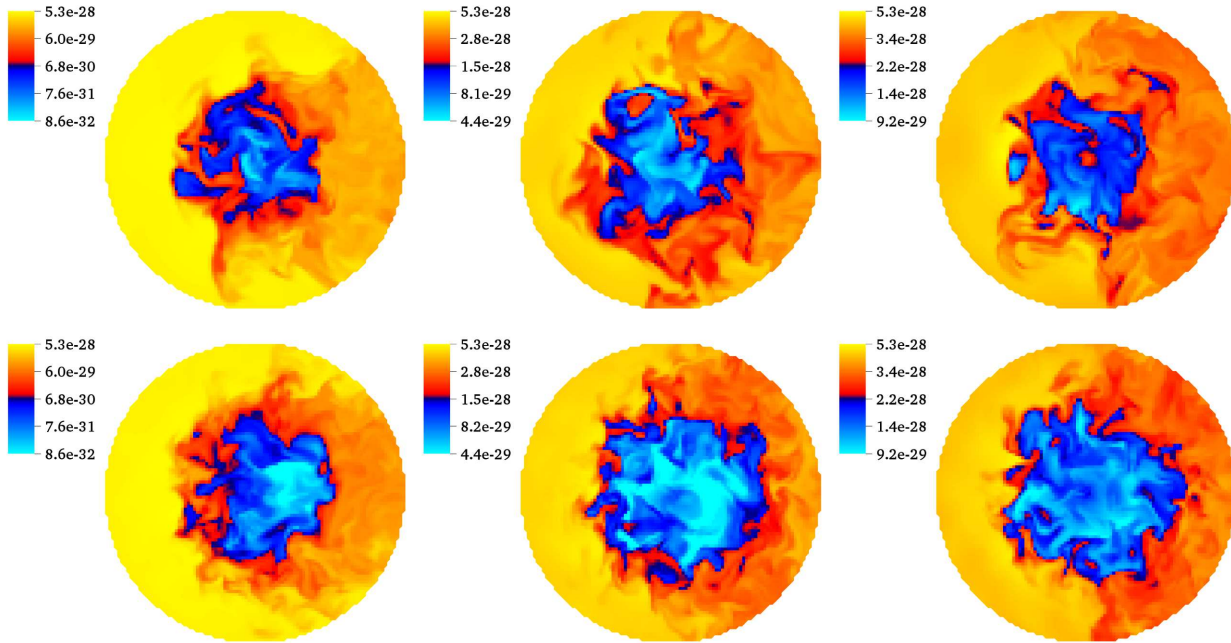


Figure A3. ICM density distributions on the x-y plane centred on the galactic centre inside R_t , and parallel to the direction of the ICM inflow. The ICM flows from left to right. Columns correspond to 2, 4.5, and 6 Gyr (*from left to right*), respectively. Top row corresponds to the original Run 5 for Case A. Bottom row shows the result for the new simulation where the turbulence driving scale is about two times smaller than the original Run 5. The unit of density is g cm^{-3} . Note that the maximum in the colour maps is fixed in all panels, while the minimum varies from left to right. The minimum density is the same for a given time to allow for straightforward comparison of the effect of the turbulence driving scale on mixing.

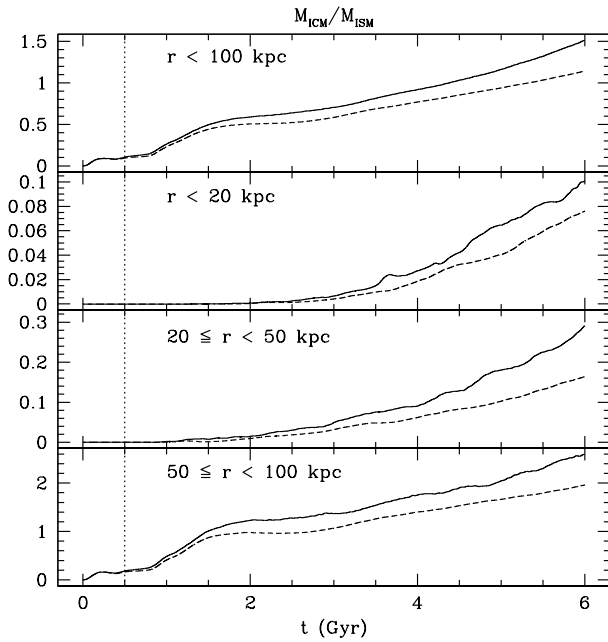


Figure A2. Evolution of the ratio of the intrinsic ICM mass to the intrinsic ISM mass inside R_t in Case A for Run 5 with smaller turbulence driving scale (*dashed line*), compared to the original run (*solid line*). The dotted line corresponds to 0.5 Gyr when the inflow of the ICM starts to enter the simulation box.